metals

MDPI

Article

Numerical and Experimental Buckling and Post-Buckling Analyses of Sphere-Segmented Toroidal Shell Subject to External Pressure

Chenyang Di [1], Jian Zhang [1,*], Fang Wang [2] and Yu Zhang [3]

[1] School of Mechanical Engineering, Jiangsu University of Science and Technology, Zhenjiang 212003, China
[2] Shanghai Engineering Research Center of Hadal Science and Technology, Shanghai Ocean University, Shanghai 201306, China
[3] School of Safety and Ocean Engineering, China University of Petroleum, Beijing 102249, China
* Correspondence: zhjian127@just.edu.cn

Abstract: This study determined the buckling characteristics of sphere-segmented toroidal shells subjected to external pressure. The proposed toroidal vessel comprises six spheres and six rings. Two laboratory models with the same nominal dimensions were manufactured, measured, tested, and evaluated. To investigate whether sphere-segmented toroidal shells are imperfection-sensitive structures with closely spaced eigenvalues, the subspace algorithm was applied to evaluate the first 50 eigenmodes, and the modified Riks algorithm was used to obtain post-buckling characteristics. The results indicated that the deviation between the results of the experimental and numerical analyses was within a reasonable range. The proposed sphere-segmented toroidal shells were highly imperfection-sensitive structures with closely spaced eigenvalues. Subsequently, imperfection sensitivity analysis confirmed this conclusion. In numerical analyses, the first eigenmode could be considered as the worst eigenmode of sphere-segmented toroidal shells. The trend of the equilibrium path of sphere-segmented toroidal shells was consistent with spherical shells, revealing instability. In addition, ellipticity and completeness exerted a negligible effect on the buckling load of sphere-segmented toroidal shells.

Keywords: sphere-segmented structure; toroidal shell; spherical shell; buckling; external pressure

Citation: Di, C.; Zhang, J.; Wang, F.; Zhang, Y. Numerical and Experimental Buckling and Post-Buckling Analyses of Sphere-Segmented Toroidal Shell Subject to External Pressure. *Metals* **2023**, *13*, 64. https://doi.org/10.3390/met13010064

Academic Editor: Matteo Benedetti

Received: 12 November 2022
Revised: 21 December 2022
Accepted: 22 December 2022
Published: 26 December 2022

1. Introduction

Toroidal shells have several advantages over traditional spherical and cylindrical shells [1], including favorable steerability, passability, and stability [2,3]. The reason for good passability is that two paths can be chosen to reach a location in toroidal shells. Toroidal shells are widely applied in ocean, nuclear, and civil industries. In ocean engineering, toroidal shells are considered to be a promising pressure structure for deep sea space stations [2,3]. However, toroidal shells have a low buckling load and are difficult to fabricate.

Buckling, which has been extensively studied, is the main type of failure affecting toroidal shells subjected to external pressure. Błachut [4] performed experiments to determine the collapse load and collapsed shape of toroidal shells. The experimental results compared well with their numerical results. Furthermore, studies have investigated the effect of the elliptical section of toroidal shells on their buckling by using the finite element method [5,6]. Zingoni proposed an approximate bending solution to solve the axisymmetric bending of elliptic toroidal shells [7]. He obtained the eigenvalues of part of the toroidal vessel by using the Galerkin's scheme to calculate stability equations [8]. Studies proposed analytical algorithms for examining the strength of ribbed toroid shells and performed a nonlinear analysis to analyze the buckling of such shells [1,9,10]. Civalek used the discrete singular convolution method to analyze the buckling of CNT-reinforced laminated non-rectangular plates [11]. Moradi-Dastjerdi analyzed the thermal and mechanical buckling of an active multidisciplinary sandwich plate by developing a mesh-free solution based on third order shear deformation theory [12].

Zhang et al. [13] designed and manufactured segmented toroidal shells composed of cylindrical shells. Furthermore, they investigated the effect of the number of segments on buckling load and imperfection sensitivity. However, it was recognized that, unlike cylindrical shells, spherical shells were more suitable for using as junction elements because the highly symmetrical structure of a spherical shell facilitated hole opening. In addition, surface stress was evenly distributed on spherical shells [14–16]. The surface of a spherical shell experienced less stress compared with other structures under the same external pressure in [17].

The combination design idea mentioned above by Zhang et al. [13] has also been used in replacing cylindrical shells with multiple intersecting spherical shells. Liang et al. [18] combined the interior penalty function and the Davidon–Fletcher–Powell method to optimize the design of multiple intersecting spheres. Subsequently, Zhang and Gou examined the effect of material and geometric parameters on the buckling of multiple intersecting spherical shells [19,20]. Liu et al. proposed an approximate analytical model for buckling analysis of common spherical–cylindrical–spherical composite structures by using the generalized Galerkin method [21]. Sobhani et al. investigated the vibration of porous nano-enriched polymer composite coupled spheroidal–cylindrical shells, the wave frequency responses of the nanocomposite linked hemispherical–conical shell, the Circumferential vibration analysis of nano-porous sandwich assembled spherical–cylindrical-conical shells, and the Free vibration of porous graphene oxide powder nano-composite assembled paraboloid–cylindrical shells [22–25]. Rezaiee and Masoodi analyzed the buckling of plates and shell structures by an efficient triangular shell element which had six nodes with thirty degrees of freedom [26]. Zingoni presented a linear–elastic theoretical formulation for determination of the state of stress in large liquid-filled multi-segmented spherical shells [27]. However, toroidal shells composed of spherical shells, termed sphere-segmented toroidal shells, have rarely been described in literature. The effects of imperfection, ellipticity, and completeness on the buckling characteristics of such structures remain unknown.

This study investigated the buckling characteristics of sphere-segmented toroidal shells under external pressure. The sphere-segmented toroidal shell could overcome the low buckling load and difficult manufacturing of the traditional toroidal shell. The advantages of the proposed experimental methodology were as follows: a pressure pump was used to increase the pressure of the chamber in hydrostatic testing, simulating the pressure under different depths and the reliability of the result could be guaranteed. On the other hand, optical scanning obtained the numerical model with initial geometrical imperfection. The accuracy of the buckling loads of the experimental model could be improved in numerical analysis. The remainder of this paper is organized as follows. Section 2 introduces the geometric properties of toroidal shells, their fabrication, and related experiments. Section 3 presents a comparison and analysis of the experimental results and the results of a finite-element analysis. In addition, the effects of ellipticity and completeness on buckling are discussed. Conclusions are presented in Section 4. This study provides valuable references for the design, manufacture, and analysis of atypical toroidal shells.

2. Materials and Methods

To experimentally evaluate the buckling of sphere-segmented toroidal shells, two models, with identical nominal dimensions and comprising six spheres and six rings, were established, named ST-1 and ST-2, respectively. The difference between ST-1 and ST-2 models were the different geometric imperfections and welding imperfections produced during the manufacturing process. Ultrasonic measurement, optical scanning, and a hydrostatic test were performed for the two models.

2.1. Geometry and Manufacture

Consider a sphere-segmented toroidal shell comprising six spheres and six rings. The spherical shell has a uniform wall thickness (t) of 0.75 mm, a radius (r) of 72.95 mm, an intersected angle (θ) of 30°, and an included angle (α) of 60°. Any two adjacent spheres are connected by a ring with a width (w) of 10 mm and a height (h) of 6 mm. The geometric notations and a photograph, of the proposed model, are presented in Figure 1. The ring dimensions were designed based on the principle of consistent deformation [19,20]. Deformation of the ring under the external pressure is consistent with the deformation of the unilaterally excised part of a spherical shell. The unilateral excision refers to the part of the spherical cap that is excised from the spherical shell. The research parameters were in direct reference to the experimental and numerical results of Zhang et al. [20]. The formula for width (w) is based on the consistent deformation principle, as reported in Equation (1):

$$w = \frac{D}{2}\left(1 - \sqrt{\frac{r^2 \sin\alpha(1-\mu)h + (\mu-1)(r\cos\alpha + h)D_r t}{r^2 \sin\alpha(1-\mu)h + (\mu+1)(r\cos\alpha + h)D_r t}}\right) \quad (1)$$

where D_r is the outer diameter of the ring, which is obtained as follows:

$$D_r = \sqrt{4(r+t)^2 - 4r^2\cos\alpha^2} \quad (2)$$

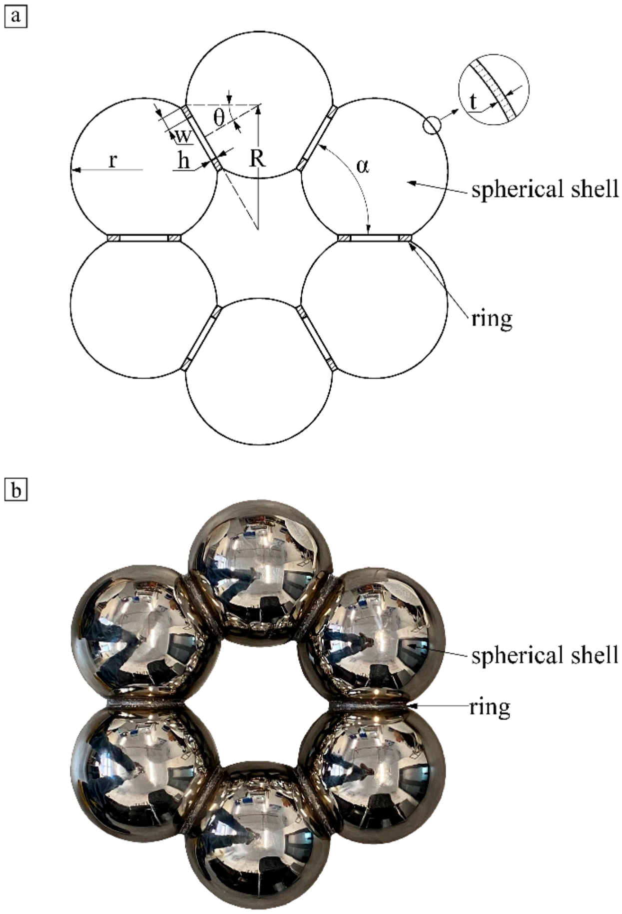

Figure 1. Geometric notations (**a**) and photograph (**b**) of a sphere-segmented toroidal shell.

The sphere-segmented toroidal shells examined herein were manufactured using stainless steel, and the corresponding material properties [16] were as follows: Young's modulus (E) = 200 GPa, Poisson's ratio (μ) = 0.291, and yield strength (σ_y) = 628 MPa. The process for manufacturing spherical shells is presented in Figure 2. First, hemispherical shells were manufactured from thin steel plates by using cold rolling technology. Second, two hemispherical shells were welded to form a complete spherical shell through manual tungsten inert gas (TIG) welding. Third, spherical shells with an included angle of 60° were cut by means of wire-cut electrical discharge machining (WEDM). To prevent repeated soldering during assembly, weld lines were located in the middle of the spherical shell during cutting. The process for manufacturing the ring shell was simple; the ring shell was directly cut from a thick steel plate through WEDM. Eventually, the cut spheres and rings were assembled, and a laboratory-scale model was obtained through manual TIG welding (Figure 1). With the use of the aforementioned fabrication process, two models were manufactured, named ST-1 and ST-2 sphere-segmented toroidal shells.

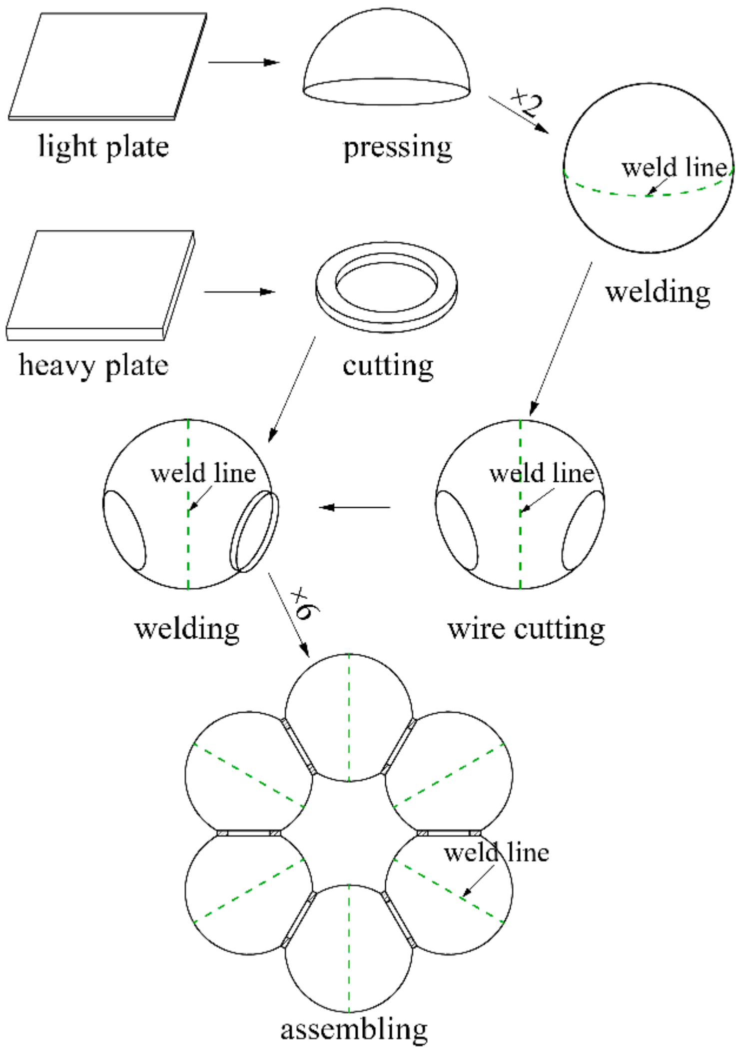

Figure 2. Schematic of the process for manufacturing sphere-segmented toroidal shells.

2.2. Geometric Measurement and Hydrostatic Testing

For the ultrasonic measurement, as presented in Figure 3a, 252 measurement points were drawn on the surface of each model. The points were located on 12 measurement lines with equal circumferential intervals. Each measurement line had 21 measurement points at equal intervals. A PX-7 ultrasonic device form DAKOTA was used to measure thickness of spheres. During the measurement, the speed of sound was set to 5664 m/s. When the demonstrated value of ultrasonic device remained unchanged and the stability indicator showed 7–8 vertical bars, the measured value was recorded. The stability indicator has 8 vertical bars in total. The statistical results for wall thickness are presented in the first five columns of Table 1.

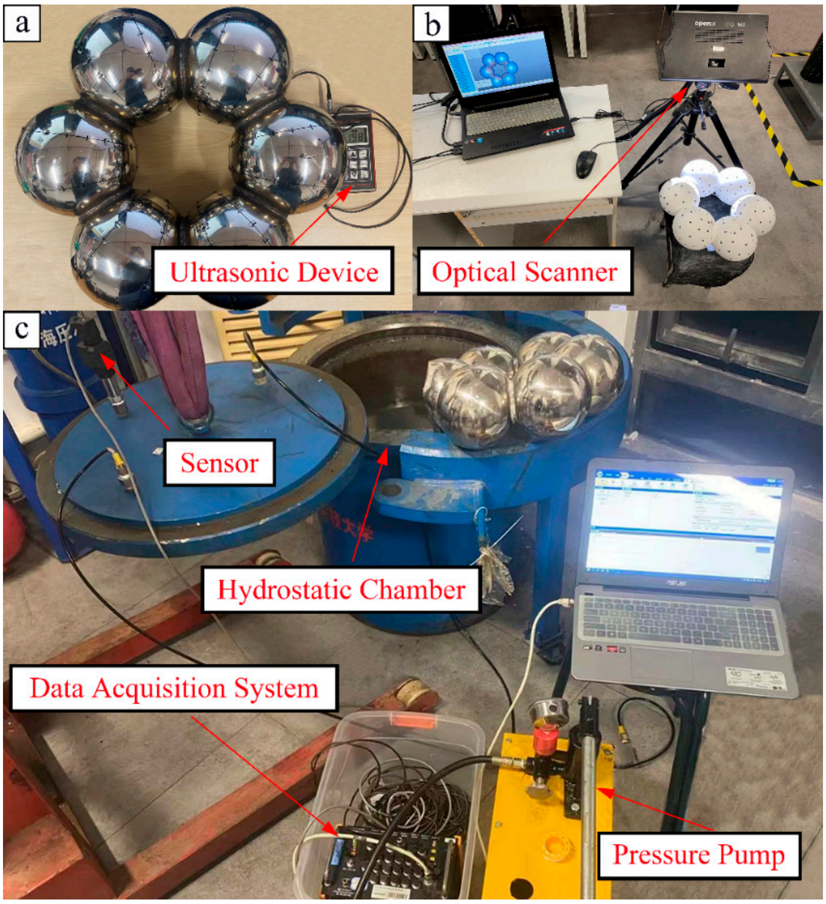

Figure 3. Photographs of ultrasonic measurement scene (**a**), optical scanning scene (**b**), and hydrostatic tests scene (**c**).

Table 1. Geometric properties, buckling load, and experiment-derived collapse pressure of ST-1 and ST-2 sphere-segmented toroidal shells.

Model	t_{min}/mm	t_{max}/mm	t_{av}/mm	St. dev.	P_{lin}/MPa	P_{non}/MPa	P_{test}/MPa	P_{non}/P_{test}
ST-1	0.686	0.826	0.753	0.037	19.206	6.229	5.523	1.128
ST-2	0.688	0.818	0.746	0.031	18.452	6.292	5.525	1.139

Note: t_{min} = minimum thicknesses; t_{max} = maximum thicknesses; t_{av} = average thicknesses; St. dev. = standard deviation of thickness; P_{lin} = linear buckling load; P_{non} = nonlinear buckling load; P_{test} = destruction load.

After the ultrasonic measurement of thickness, the measurement points were erased using absolute alcohol (99.9% alcohol) from Shanghai Yishida (Shanghai, China). Three-dimensional coordinates of two models were revealed using the Cronos 3D optical scanner from Open Technologies (Brescia, Italy) and three-dimensional data for sphere-segmented toroidal shells were reconstructed using the device's supporting software. The technical parameters of the aforementioned scanner were as follows: scanning range = 150 × 115 × 150 mm^3, pixel size = 200 m, working distance = 310 mm, and accuracy = 0.02 mm. To ensure scanning quality and efficiency, spacing between marked measurement points was set to 3–5 mm. Additional details on optical scanning are presented in Figure 3b. The geometric deviations of scanned models from perfect geometries are presented in Figure 4.

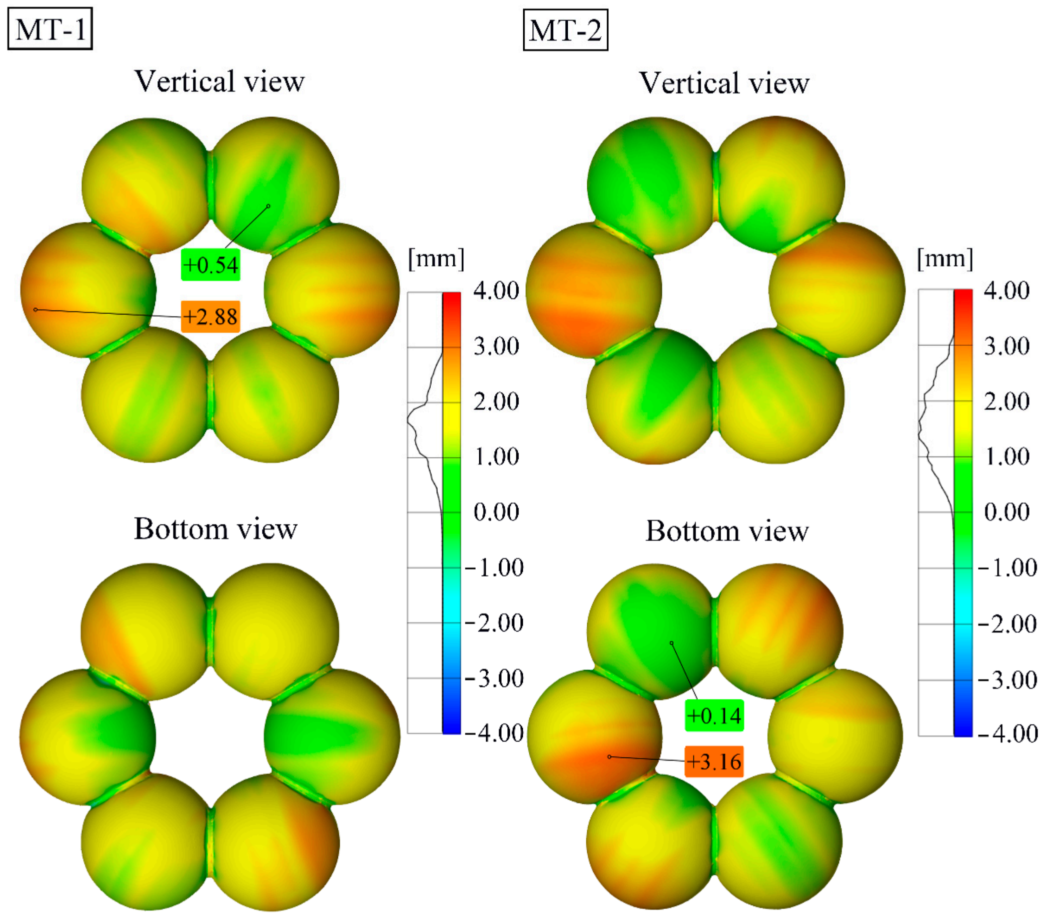

Figure 4. Geometric deviation between the scanned models and perfect geometries of two laboratory models sphere-segmented toroidal shells (named ST-1 and ST-2, respectively).

When shape and thickness measurements were complete, hydrostatic pressure tests were performed in a hydrostatic chamber. The chamber was located at the Jiangsu Provincial Key Laboratory of Advanced Manufacturing for Marine Mechanical Equipment, as presented in Figure 3c. The chamber has an inner diameter of 500 mm and a height of 500 mm, with a working pressure of 20 MPa (equivalent to a water depth of 2000 m). To reduce perturbance from buoyancy, a weight was attached to each model by using a soft rope to ensure the model floated in the middle part of the pressure chamber. After chamber air was exhausted and the measured pressure was removed, the pressure history was recorded using a DH5902N dynamic data acquisition system from Donghua Test (Taizhou, China). This system features built-in various bridge sensors, which can test and analyze physical quantities, such as pressure, force, load, displacement, etc. The dynamic data acquisition system, with an IP65 rating for protection, had impact resistance of 100 g and a working temperature range of −20 °C to 60 °C. In the acquisition process of pressure, a SUP-P300 sensor from Meiyi Automation Company (Hangzhou, China) was used for pressure measurement. The sensor's range was 0–10 MPa, and its accuracy level was 0.5%. The acquisition frequency was set to 50 Hz. Collapse was indicated by a loud noise from collapse of the model. Zhang et al. [28] provided detailed instructions on equipment operation of the hydrostatic chamber. The recorded pressure history is presented in Figure 5, and the collapse of the model after the hydrostatic test is presented in Figure 6.

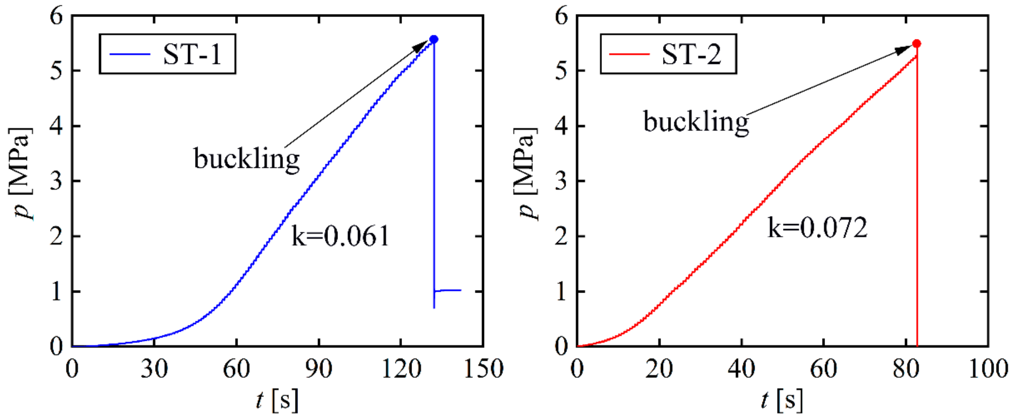

Figure 5. Pressure versus time curves for ST-1 and ST-2 sphere-segmented toroidal shells under uniform external pressure.

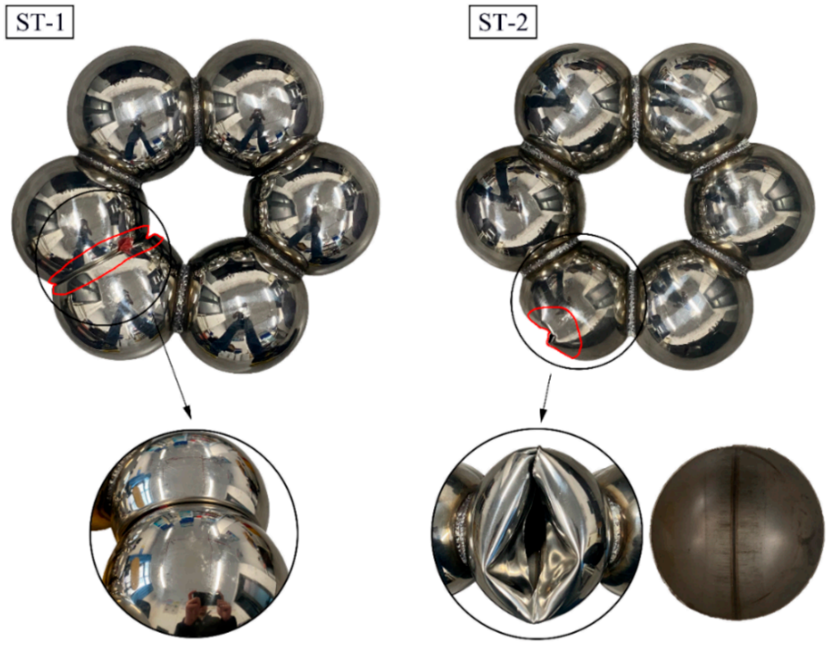

Figure 6. Failed sphere-segmented toroidal shell and collapse locations.

3. Results and Discussion

This section presents an evaluation and comparison of experimental and numerical results derived from the two proposed models. Closely spaced eigenvalue analyses and nonlinear buckling analyses were performed on the perfect geometries of sphere-segmented toroidal shells; this enabled an exploration of whether the first-order eigenmode was consistent with the worst eigenmode. Furthermore, the effect of ellipticity and completeness on sphere-segmented toroidal shell buckling was explored.

3.1. Experimental Analysis of the Two Sphere-Segmented Toroidal Shells

The manufactured sphere-segmented toroidal shells exhibited satisfactory and repeatable thickness distributions. The minimum thicknesses of the two spheres were 0.686 and 0.688 mm, respectively, and their maximum thicknesses were 0.826 and 0.818 mm, respectively (Table 1). The standard deviation of thickness ranged from only 0.031 to 0.037. The results indicated that cold rolling technology could be applied to obtain spheres of uniform thickness.

The overall accuracy and repeatability of the sphere-segmented toroidal shells were reasonable. The geometric and extreme deviations of the two models (not including welds) ranged from 0 to 3 mm and from 0.14 to 3.16 mm, respectively (Figure 4). However, the manufactured toroidal shells inevitably had some imperfections. Local pits might arise at the junctions of the spheres and rings because of welding deformation. Additionally, as depicted in the vertical view of Figure 4, a large deviation was present in the horizontal direction of the shells and a small deviation in the vertical direction, presenting an overall appearance of ellipticity. Such ellipticity exerted a negligible effect on the buckling load on sphere-segmented toroidal shells (see Section 3.3 for further discussion).

A slow increase in pressure corresponded to the quasi-static loading of the sphere-segmented toroidal shells (Figure 5). The slowly increasing pressure was used to simulate the shell under different water depths. In Figure 5, the factor k was the ratio of pressure to time. The factor k of ST-1 and ST-2 ranged from 0.061–0.072 MPa/s. A manual pressure pump was used to slowly increase the pressure in the chamber and the process was uniform and slow without sudden changes. In this study, the time of the twice conducted process of slow increase of pressure was 83 s and 132 s, respectively. The pressure peak corresponded to the collapse pressure of the two manufactured samples. The corresponding results are presented in the penultimate column of Table 1. The pressure data from hydrostatic tests on ST-1 and ST-2 sphere-segmented toroidal shells are presented in Figure 5. For ST-1, when the pressure reached 5.523 MPa, it dropped markedly until it reached a stable level. Similarly, for ST-2, when the pressure reached 5.525 MPa, it rapidly dropped to zero. The sudden drop of pressure of ST-1 and ST-2 represented deformation in the fabricated models. The trend of dropping to zero and the trend of reaching a stable level indicated that elastic–plastic deformation occurred. The buckling loads of ST-1 and ST-2 sphere-segmented toroidal shells were almost the same, with a deviation of less than 1%.

The significant difference of collapse between ST-1 and ST-2 sphere-segmented toroidal shells was ascribed to different geometric imperfections and different thicknesses after manufacturing. The collapse shapes of ST-1 and ST-2 sphere-segmented toroidal shells from different viewpoints are presented in Figure 6. ST-1 collapsed near the ring, which was typical for a hemisphere subjected to external pressure [29–31]. This phenomenon might have arisen due to abrupt stiffness and geometric imperfections. The collapsed shape of ST-2 was more common than that of ST-1. The collapse of ST-2 occurred on the equator of the sphere. The tearing mode at the collapse site was associated with the equator thinning. When the amplitude of this imperfection was small, it did not affect the buckling load [32].

3.2. Numerical Analysis of the Two Manufactured Sphere-Segmented Toroidal Shells

According to the Design of Steel Structures (European Union code) and Rules for the Classification and Construction of Diving Systems and Submersibles [33,34], the buckling of the sphere-segmented toroidal shells was further analyzed using the finite-element method. Linear and nonlinear buckling characteristics were determined using the subspace iteration algorithm and modified Riks algorithm [35] in ABAQUS, respectively. During the calculation, a reference load of 1 MPa was applied to the surface of each model.

The finite-element models and information on the sphere-segmented toroidal shells are presented in Figure 7. The white and green parts correspond to rings and spheres, respectively. The geometrical shape of ST-1 and ST-2 sphere-segmented toroidal shells obtained using optical scanning was segmented and adjusted in Unigraphics NX. The height of the ring was set exactly to 6 mm, which was the same height as that of the ring discussed in Section 2.1. The spheres and rings at joint shared common nodes. A three-point boundary was used to prevent the additional displacement of the sphere-segmented toroidal shells. On the extrados of the toroidal shells, two points of boundary were selected to limit the displacement of the X and Z axes ($U_X = U_Z = 0$). On the symmetrical plane of the ring, which was not collinear with the previous two points, one point was selected to limit the displacement of the X and Y axes ($U_X = U_Y = 0$). The aforementioned method was applied to examine the buckling of egg-shaped shells [36,37], longan-shaped shells [38], spherical shells [39,40], and toroidal shells [41,42]. Due to the complexity of the surfaces of sphere-segmented toroidal shells, most of the elements were set to be quadrangular shell elements (S4). These elements were fully integrated, general purpose, finite membrane strain shells. A proportion of elements were set to be triangular shell elements (S3). Triangular shell elements (S3) use reduced integration. The size of mesh was defined in ANSA, and the length parameter was 4.5. The representative examples of convergence study of ST-1 sphere-segmented toroidal shells are displayed in Figure 7. The red dot represents the determined element quantity intended for the numerical analysis. The convergence study was based on the eigenmode analysis.

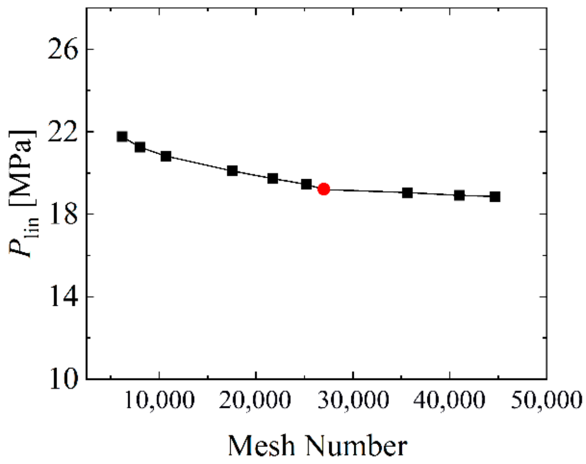

Figure 7. Convergence study of ST-1 sphere-segmented toroidal shell.

The number of each type of element and the number of nodes for ST-1 and ST-2 sphere-segmented toroidal shells are presented in Figure 8. The parameters for analysis, based on the subspace algorithm, were as follows: number of eigenvalues requested = 6, vectors used per iteration = 12, and maximum number of increments = 3000. The parameters for analysis, based on the modified Riks algorithm, were as follows: maximum incremental steps = 300, initial arc length = 0.08, minimum arc length = 1×10^{-5}, and maximum arc length = 0.08. The numerical analysis results are presented in columns 6 and 7 of Table 1 and Figures 9 and 10.

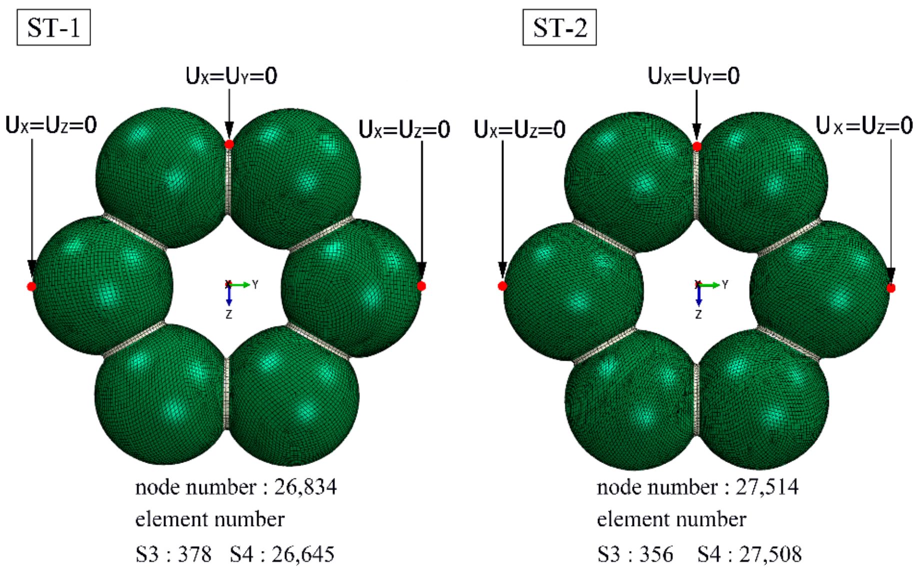

Figure 8. Finite-element models of sphere-segmented toroidal shells and relevant information.

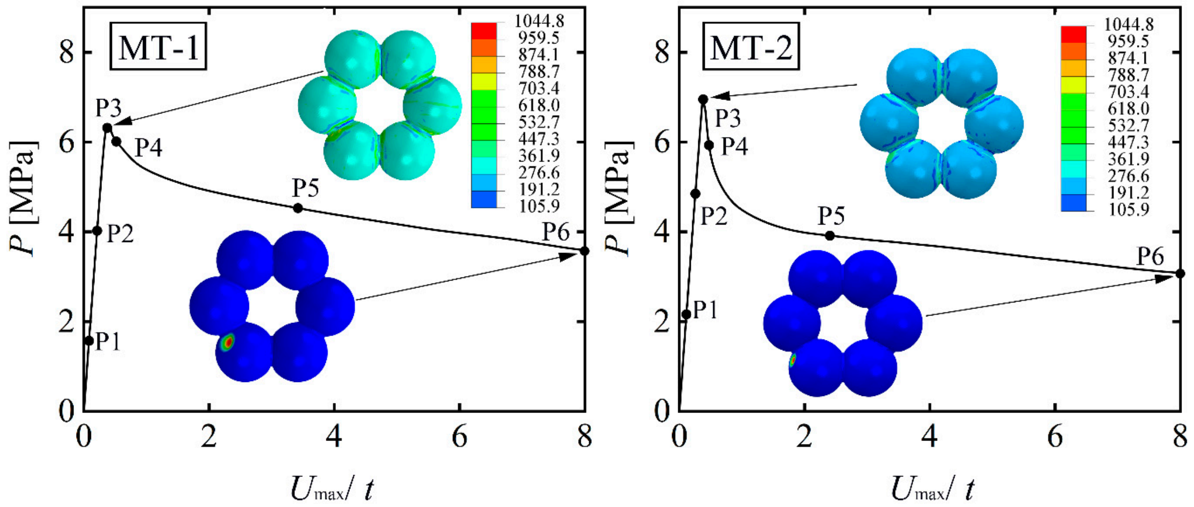

Figure 9. Equilibrium paths, stress distribution, and post-buckling modes of ST-1 and ST-2 sphere-segmented toroidal shells.

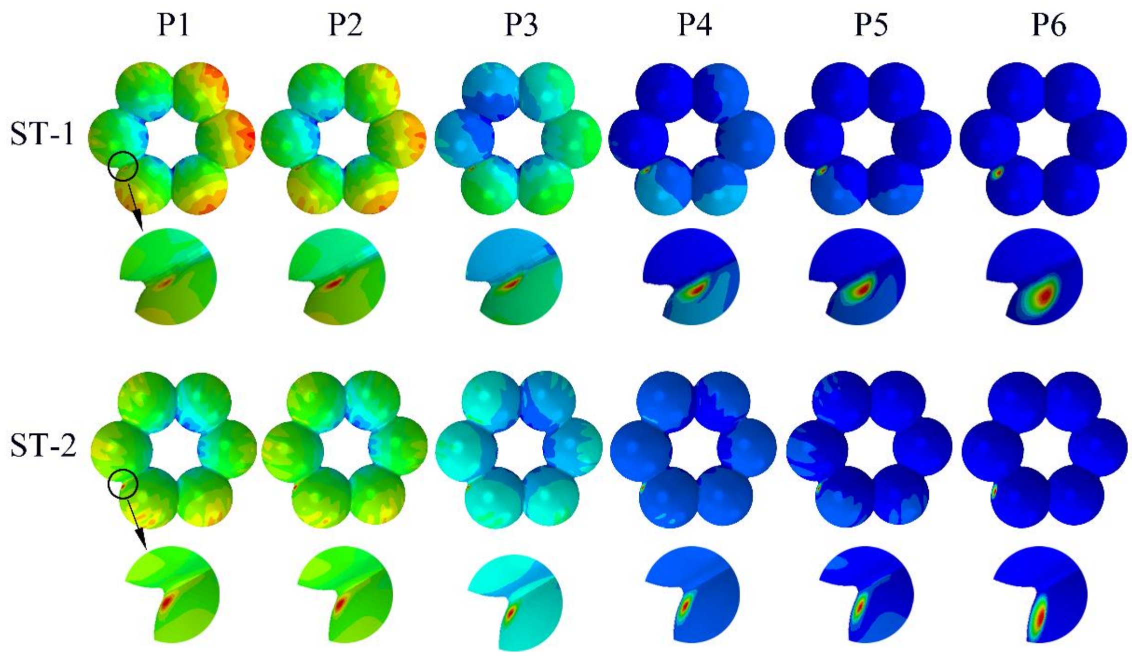

Figure 10. Deformation evolution of ST-1 and ST-2 sphere-segmented toroidal shells; six points correspond to those in Figure 9.

The numerical buckling loads had high repeatability and reasonable accuracy. Linear and nonlinear analysis was based on the real geometric shape from data of ultrasonic measurement, which could help in exploring the mechanism of the collapse behavior of the fabricated models. As indicated in Table 1, the nonlinear buckling loads of ST-1 and ST-2 sphere-segmented toroidal shells were 6.229 and 6.292 MPa, respectively. The linear buckling load ratio between ST-1 and ST-2 sphere-segmented toroidal shells was 1.04, and the nonlinear buckling load ratio between ST-1 and ST-2 sphere-segmented toroidal shells was 0.92. These results indicated that the numerical results related to the manufactured samples had high repeatability. The deviation between the numerical and experimental results ranged from 12.8% to 13.9%, indicating that the numerical results had reasonable accuracy.

The sphere-segmented toroidal shells had an unstable structure. As presented in Figure 9, the path curve increased linearly during the pre-buckling stage, and during the post-buckling stage the path curve exhibited a sharp drop and then a slow drop. P3 was the critical buckling load point, and other points could represent the intermediate deformation evolution of the aforementioned shell. Maximum stress in stress distribution exceeded the yield strength at the buckling point, indicating elastic–plastic buckling.

The sphere and ring junction was the weakest position in ST-1 and ST-2 sphere-segmented toroidal shells. The deformation states of the two models are presented in Figure 10 and correspond to the six points in Figure 9. The ellipticity discussed in Section 2.2 eliminated the high symmetry of the sphere-segmented toroidal shells, resulting in an uneven force on the extrados and culminating in local pre-buckling deformation. After the critical buckling point was reached, instability eventually occurred at the aforementioned junction. Local dents could be observed at the same position in Figure 4, and the stress distribution in Figure 9 indicated that this position was the weakest.

The collapse position of the numerical analysis and hydrostatic test of ST-1 was consistent. The collapse of local dents occurred at the junction of the sphere and ring. The numerical analysis results differed from the hydrostatic test, because the welding imperfections, stiffness, geometric properties, and thickness were different in the collapse location. Since welding was incomplete, the shell model had thickness–related imperfections [32]. Moreover, when the thinning of the welded seam was small, the buckling load of the aforementioned shells was negligibly affected.

3.3. Experimental Analysis of the Two Sphere-Segmented Toroidal Shells

To examine the buckling of sphere-segmented toroidal shells, eigenmodes were introduced into the perfect model as an initial geometric imperfection. Subsequently, a nonlinear analysis was performed on the perfect model with eigenmode imperfections.

In any analysis of the buckling characteristics of shells, the effect of worst-case imperfections must be considered [43–46]. The first eigenmode is typically a good estimate of the worst shape [47]. This method of analysis is recommended under European Union and Chinese regulations [33,34]. The aforementioned method has been successfully applied for analyzing the buckling characteristics of corrugated cylindrical and spherical shells [48,49]. However, sphere-segmented toroidal shells are atypical toroidal shells; they are composed of spheres and rings. Numerous studies have indicated that spherical, toroidal, and cylindrical shells have imperfection-sensitive structures under symmetrical load conditions [13,40,50]. Hutchinson indicated that shells composed of cylindrical and spherical structures are the most sensitive to imperfection among all structures [51]. Therefore, the first 50 eigenmodes should be obtained by performing a linear eigenvalue analysis, and nonlinear buckling under each eigenmode should then be analyzed. Whether the first mode can replace the worst mode as an eigenmode imperfection in a nonlinear analysis requires further discussion. The boundary conditions and parameter settings were the same as in Section 3.2. The imperfection amplitudes were set as 0.1 t in Section 3.3.

Small deviations in adjacent order eigenvalues and repeated eigenvalues demonstrated that the sphere-segmented toroidal shells had an imperfection-sensitive structure with closely spaced eigenvalues. Table 2 presents the first 50 eigenmodes and linear buckling loads for perfect sphere-segmented toroidal shells, and the corresponding statistical results are presented in the first row of Table 3. The linear buckling load varied from 26.549 to 26.758 MPa, the standard deviation in linear buckling load was only 0.067, and the average linear buckling load was 26.645 MPa (Table 3). As presented in Figure 11a, the ordinate was the ratio of the linear buckling loads of each order to the first order. The ratio of linear buckling loads of the 50th order to the 1st order was 1.0079. In addition, because of the presence of the same eigenvalues, the minimum deviation of the eigenvalues of adjacent orders was 0. The maximum deviation was 0.0038%, which was observed between the ninth and tenth order.

Table 2. First 50th linear buckling loads and eigenmodes of sphere-segmented toroidal shells.

Order	**1st Mode**	**2nd Mode**	**3rd Mode**	**4th Mode**	**5th Mode**	**6th Mode**	**7th Mode**	**8th Mode**	**9th Mode**
P_{lin}	26.549	26.550	26.550	26.551	26.557	26.558	26.558	26.564	26.564
Mode	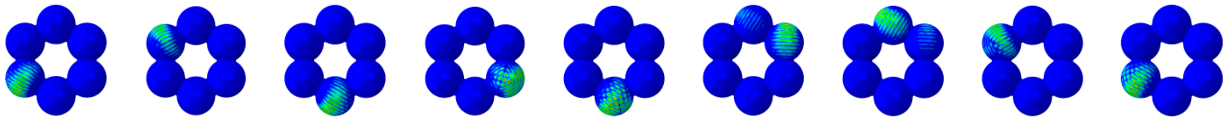								
Order	**10th Mode**	**11th Mode**	**12th Mode**	**13th Mode**	**14th Mode**	**15th Mode**	**16th Mode**	**17th Mode**	**18th Mode**
P_{lin}	26.577	26.579	26.586	26.586	26.586	26.594	26.594	26.595	26.601
Mode	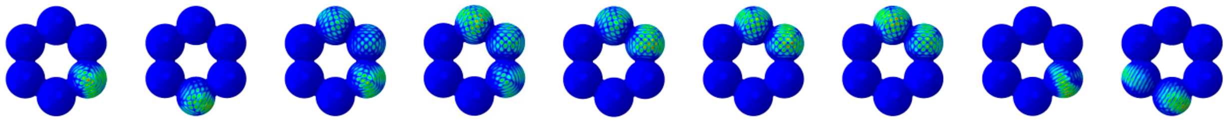								
Order	**19th Mode**	**20th Mode**	**21st Mode**	**22nd Mode**	**23rd Mode**	**24th Mode**	**25th Mode**	**26th Mode**	**27th Mode**
P_{lin}	26.602	26.602	26.602	26.603	26.612	26.612	26.657	26.657	26.667
Mode	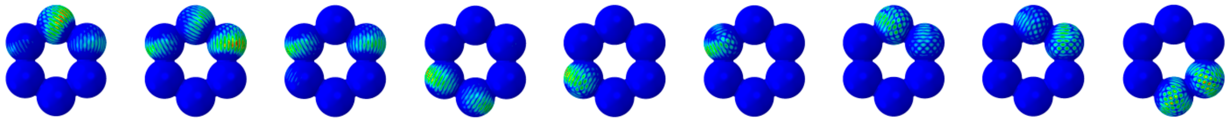								
Order	**28th Mode**	**29th Mode**	**30th Mode**	**31st Mode**	**32nd Mode**	**33rd Mode**	**34th Mode**	**35th Mode**	**36th Mode**
P_{lin}	26.667	26.674	26.678	26.678	26.682	26.682	26.690	26.690	26.691
Mode	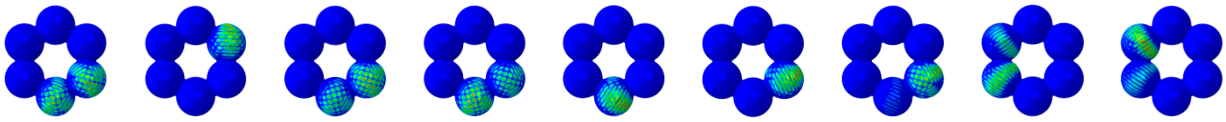								
Order	**37th Mode**	**38th Mode**	**39th Mode**	**40th Mode**	**41st Mode**	**42nd Mode**	**43rd Mode**	**44th Mode**	**45th Mode**
P_{lin}	26.691	26.694	26.708	26.708	26.713	26.714	26.727	26.732	26.737
Mode	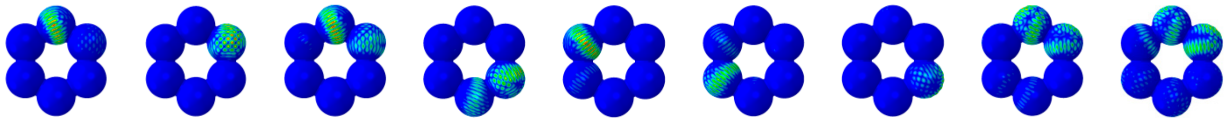								
Order	**46th Mode**	**47th Mode**	**48th Mode**	**49th Mode**	**50th Mode**				
P_{lin}	26.746	26.746	26.750	26.757	26.758				
Mode	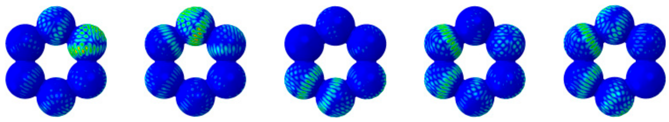								

Table 3. Statistical results related to linear and nonlinear buckling loads (see Tables 2 and 4).

Model	P_{min}**/mm**	P_{min}**/mm**	P_{av}**/mm**	**St. dev.**
P_{lin}	26.549	26.758	26.645	0.067
P_{non}	9.922	10.668	10.394	0.155

The post-buckling modes of the sphere-segmented toroidal shells were all localized dents. However, the local instability position presented stochastics, because it was affected by closely spaced eigenvalues. The nonlinear buckling loads are presented in the first line of Table 4, and the corresponding post-buckling modes of toroidal shells are presented in the second line of Table 4. The seventh mode was the worst, and the corresponding buckling load was a maximum value of 9.922 MPa. The 43rd mode was the best, and the corresponding buckling load was a minimum value of 10.668 MPa.

Table 4. Post-buckling modes and nonlinear buckling loads of sphere-segmented toroidal shells (the results correspond to the data in Table 2).

Order	**1st Mode**	**2nd Mode**	**3rd Mode**	**4th Mode**	**5th Mode**	**6th Mode**	**7th Mode**	**8th Mode**	**9th Mode**
P_{non}	10.150	10.349	10.352	10.543	10.370	10.379	9.922	10.236	10.474
Mode	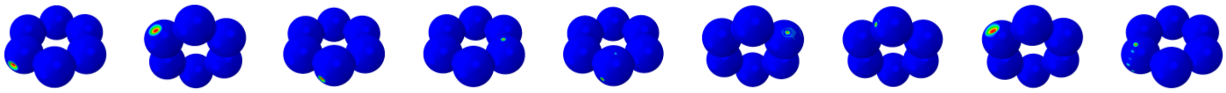								
Order	**10th Mode**	**11th Mode**	**12th Mode**	**13th Mode**	**14th Mode**	**15th Mode**	**16th Mode**	**17th Mode**	**18th Mode**
P_{non}	10.575	10.234	10.388	10.451	10.370	10.440	10.454	10.601	10.243
Mode	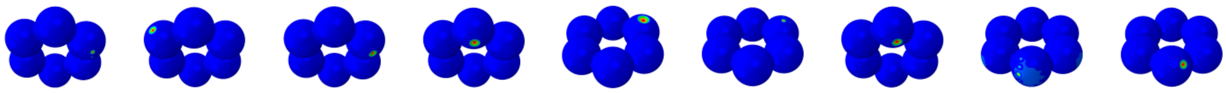								
Order	**19th Mode**	**20th Mode**	**21st Mode**	**22nd Mode**	**23rd Mode**	**24th Mode**	**25th Mode**	**26th Mode**	**27th Mode**
P_{non}	10.292	10.439	10.274	10.281	10.271	10.265	10.431	10.458	10.538
Mode	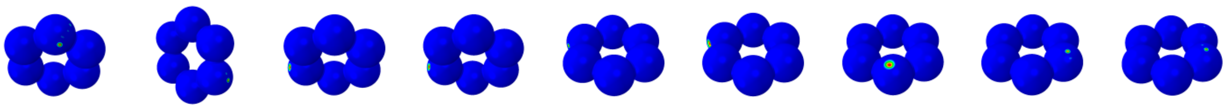								
Order	**28th Mode**	**29th Mode**	**30th Mode**	**31st Mode**	**32nd Mode**	**33rd Mode**	**34th Mode**	**35th Mode**	**36th Mode**
P_{non}	10.541	10.403	10.452	10.479	10.073	10.089	10.567	10.504	10.582
Mode	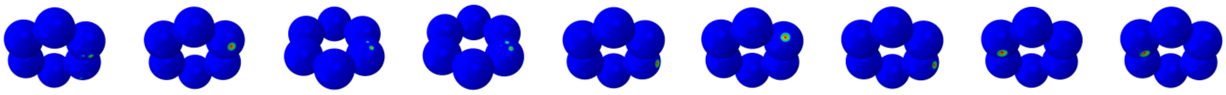								
Order	**37th Mode**	**38th Mode**	**39th Mode**	**40th Mode**	**41st Mode**	**42nd Mode**	**43rd Mode**	**44th Mode**	**45th Mode**
P_{non}	10.521	10.342	10.509	10.283	10.584	10.489	10.668	10.534	10.367
Mode	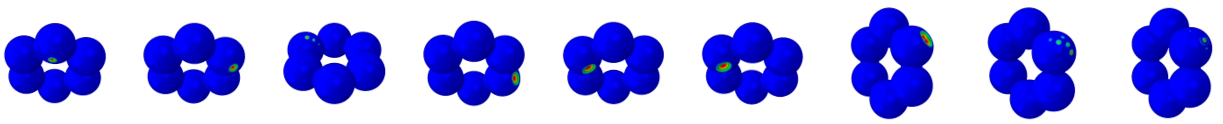								
Order	**46th Mode**	**47th Mode**	**48th Mode**	**49th Mode**	**50th Mode**				
P_{non}	10.367	10.457	10.106	10.453	10.532				
Mode	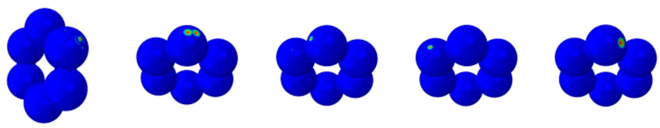								

The deviation between the buckling load of the first mode and the buckling load of the worst mode was only 2.2%, indicating that the first mode could be considered the worst mode for use as an eigenmode imperfection in a nonlinear analysis. As presented in Figure 11b, the curve was the ratio of the nonlinear buckling load under the first-order eigenmode imperfection to the nth-order eigenmode imperfection. The ratio was mostly slightly above 1 when the order was from 1–50.

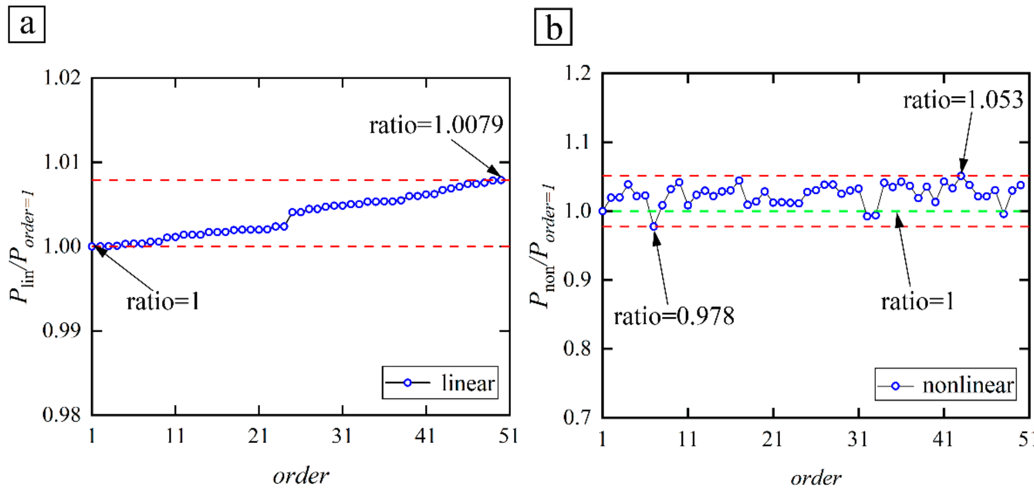

Figure 11. Normalized linear and nonlinear buckling loads for sphere-segmented toroidal shells.

To further prove that the sphere-segmented toroidal shell is an imperfection-sensitive structure, an imperfection sensitivity analysis was conducted on the shell. The imperfection amplitude was in the range of 0–1.2 t, and a total of 13 imperfection amplitudes were selected for the analysis. The calculation results are presented in Figure 12a. On the basis of the finding that the first mode could be considered the worst one, the analysis method adopted was based on first-order eigenmode imperfections. The knockdown factor was the ratio of the nonlinear buckling load under the first eigenmode imperfection to the nonlinear buckling load of the perfect model. As can be seen from Figure 12a, the knockdown factor decreased from 0.824 to 0.442, with the imperfection size increasing from 0.1 t to 0.5 t, indicating that the sphere-segmented toroidal shell was a highly imperfection-sensitive structure. Under small imperfection, the curve of the imperfection analysis had a high slope. Instead, under large imperfection, the curve had a low slope. These findings indicated decrease of imperfection sensitivity of the sphere-segmented toroidal shell with increase of imperfection size.

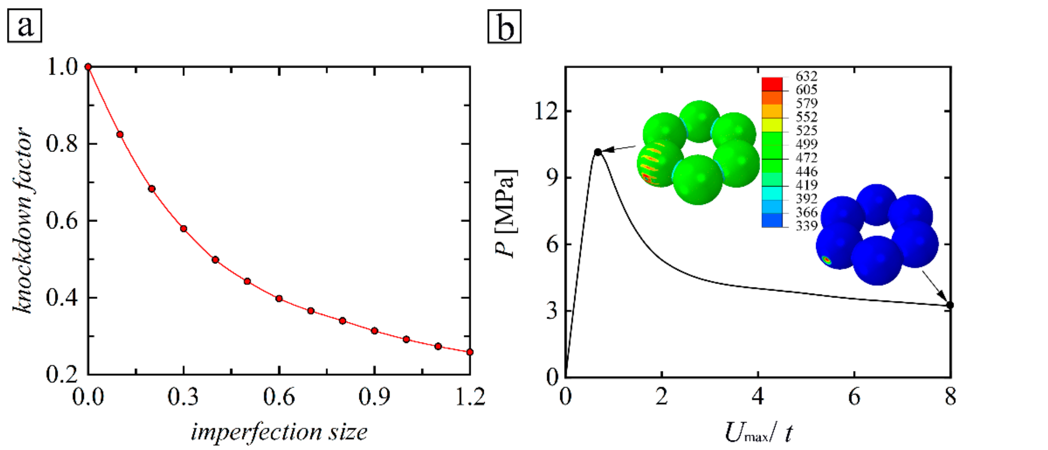

Figure 12. Imperfection sensitivities (**a**) and equilibrium path (**b**) of sphere-segmented toroidal shell.

As indicated in Figure 12b, the equilibrium path of the imperfect model is similar to the experimental model, and both show an unstable post-buckling path. The maximum stress exceeded the yield strength, indicating the occurrence of elastoplastic instability. This finding was consistent with those of the experiments. Moreover, the post-buckling mode of ST-1 was similar to that of the ideal model. These results demonstrated that a nonlinear analysis with the introduction of modal imperfections could be used for the preliminary investigations of the buckling of sphere-segmented toroidal shells.

3.4. Effect of Elliptic Imperfections on Sphere-Segmented Toroidal Shells

To study the effect of elliptic imperfections on the buckling of sphere-segmented toroidal shells, six sets of ellipses were selected, namely, 1, 1.024, 1.047, 1.066, 1.083, 1.095, and 1.104, for the finite-element analysis, and the analysis method was the same as that described in Section 3.2. As presented in Figure 13a, the ellipse passed through the center of all the spherical shells; the long semi-axis of the ellipse was denoted as a, and the short semi-axis of the ellipse was denoted as b. Notably, the definition of ellipticity was determined without rings because the values of the semi-axes, a and b, could be defined more efficiently without rings. Ellipticity was caused by a deviation in the included angles β and γ (Figure 13b) during manufacturing. Detailed geometric parameters are listed in columns 1 to 5 of Table 5.

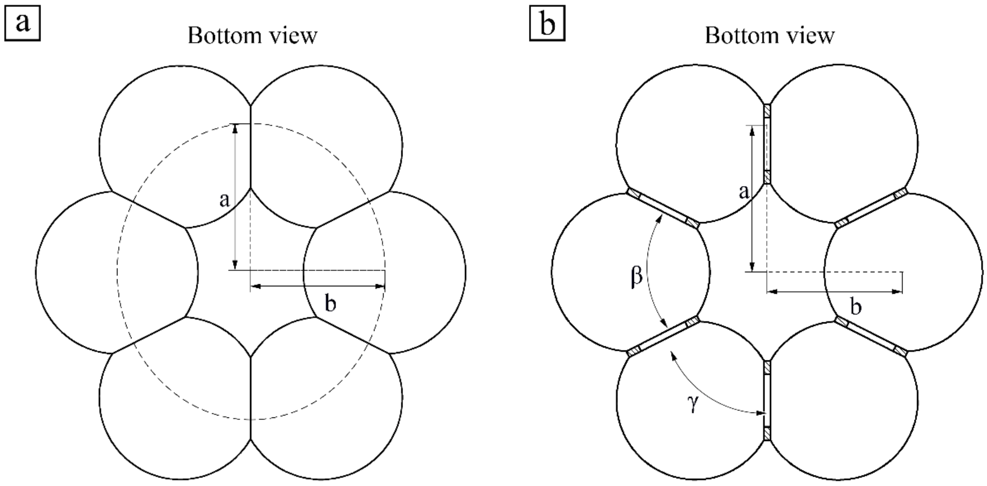

Figure 13. (**a**) Geometric notations for sphere-segmented toroidal shells under the influence of ellipticity. (**b**) Ellipticity parameter definition diagram.

Table 5. Geometrical parameters and buckling loads of sphere-segmented toroidal shells with different ellipticities (K).

K	α	β	a	b	P_y	P_{non}	P_{inon}
1	60.00	60.00	126.35	126.35	11.505	12.615	10.398
1.024	60.79	58.42	127.87	124.84	11.584	12.548	10.412
1.047	61.50	57.01	129.22	123.44	11.582	12.666	10.540
1.066	62.10	55.80	130.41	122.3	11.089	12.548	10.334
1.083	62.59	54.85	131.40	121.37	11.504	12.507	10.497
1.095	62.96	54.07	132.12	120.61	11.682	12.669	10.446
1.104	63.21	53.57	132.59	120.14	11.681	12.600	10.565

As presented in Figure 14, the linear buckling of a sphere-segmented toroidal shell occurred on the symmetry plane of that shell, which was the farthest part from the two adjacent rings. Although the ring had an equivalent stress distribution to that of the resected spherical shell, the difference in stiffness between the ring and sphere caused a transfer of weak areas. Figure 14 reveals that the instability position of the shell was not fixed on the major or minor semi-axis; instead, the position was stochastic. This stochastic position was consistent with the linear analysis results in Table 2, indicating that ellipticity had little effect on the instability position of a sphere-segmented toroidal shell.

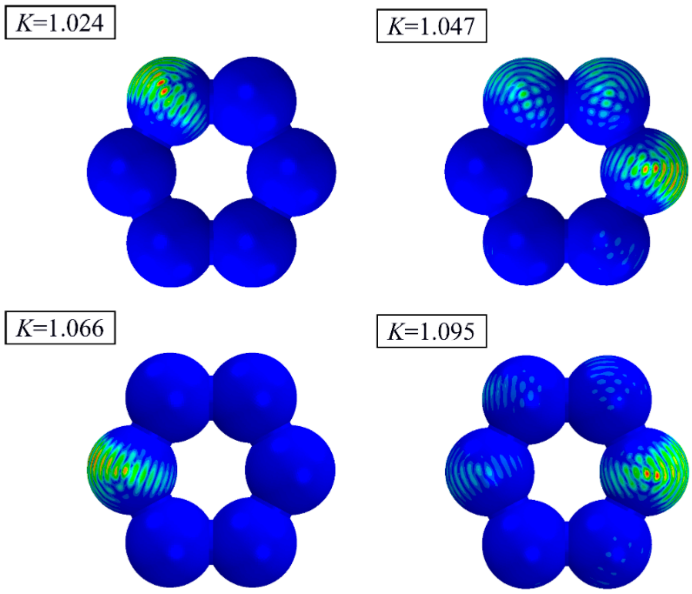

Figure 14. First-order eigenmode of sphere-segmented toroidal shells with ellipticity (K) of 1.024, 1.066, 1.083, and 1.095.

The trend of the equilibrium paths of the four models was consistent with the results in Section 3.2 and all equilibrium paths of the four models exhibited instability. The post-buckling modes and equilibrium paths of the four sphere-segmented toroidal shells, that were representative, under the effect of ellipticity are presented in Figure 15. The post-buckling instability position was on the symmetry plane of the spherical shell; this position differed from that in experimental results. This result indicated the instability position of ST-1 was not affect by the effect of ellipticity.

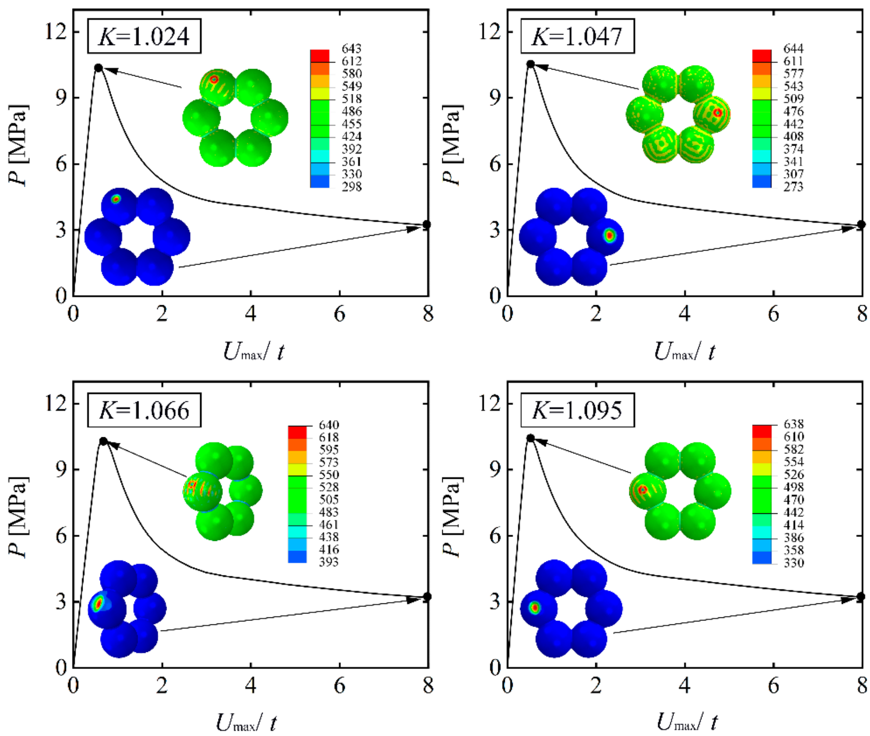

Figure 15. Equilibrium paths of sphere-segmented toroidal shells with ellipticity of (K) = 1.024, 1.066, 1.083, and 1.095.

The buckling of sphere-segmented toroidal shells was negligibly affected by ellipticity. The effect of ellipticity on the first yield load P_y, the nonlinear buckling load without imperfection P_{non}, and the nonlinear buckling loads with the eigenmode imperfection P_{inon} are presented in Figure 15. Detailed values are listed in the last three columns of Table 5. As presented in Figure 15, at an approximate ellipticity (K) of 1.047, the curve of the first yield load exhibited a small fluctuation. Compared with at an ellipticity (K) of 1, the deviations among three type loads of sphere-segmented toroidal shells under the influence of ellipticity were in the range of 0.1%–3.6%.

3.5. Effect of Completeness Imperfections on Sphere-Segmented Toroidal Shells

To study the effect of completeness on sphere-segmented toroidal shells, the finite-element analysis method, described Section in 3.2, was conducted on toroidal shells with a segment number (n) of 1–6. The first eigenmodes obtained from the subspace algorithm are presented in Figure 16 and the corresponding postbuckling modes are presented in Figure 17. The critical buckling loads and first yield loads of sphere-segmented toroidal shells with different segment numbers are presented in Table 6.

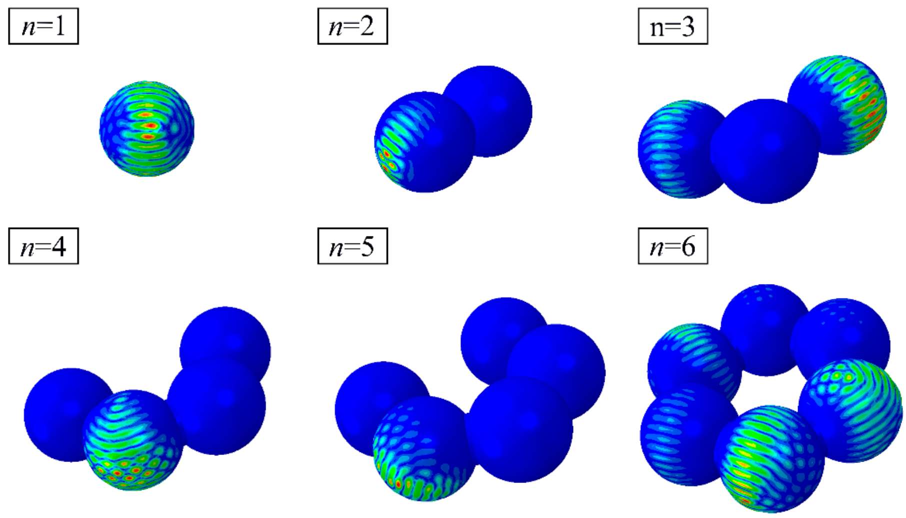

Figure 16. First-order eigenmode of sphere-segmented toroidal shells with a segment number of 1–6.

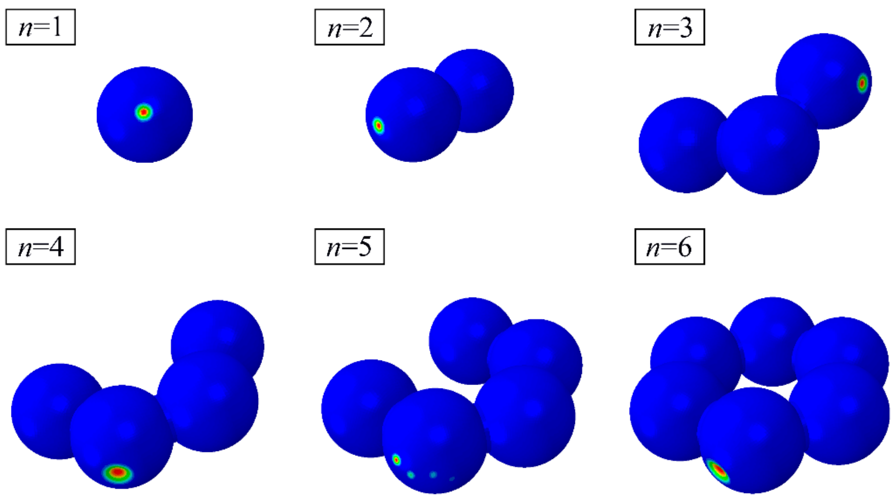

Figure 17. Post-buckling modes of sphere-segmented toroidal shells (n = 1–6) correspond to Figure 16.

Table 6. First yield load (P_y) and nonlinear buckling load (Δ = 0 and 0.1 t) for sphere-segmented toroidal shells with a segment number (n) of 1–6.

	n = 1	n = 2	n = 3	n = 4	n = 5	n = 6
P_y	12.007	11.635	11.362	11.491	11.651	11.505
Δ = 0	12.753	12.350	12.585	12.431	12.420	12.615
Δ = 0.1 t	10.483	10.381	10.244	10.186	10.492	10.398

The eigenmode of a sphere-segmented toroidal shell with different segment numbers took the form of multiple waves, as presented in Figure 16. This finding was consistent with the linear analysis results for a single spherical shell [51]. The instability position was not affected by the number of segments and the position was stochastic. Zhang et al. explored the effect of completeness on toroidal shell segments [42]. The results revealed that the buckling load increased with the rotation angle. The difference between the results of the present study and those of Zhang et al. arise from the distinct design principles of sphere-segmented toroidal shells [20], which is represented by the consistent deformation principle.

The post-buckling modes that correspond to linear buckling locations all indicated localized buckling. As presented in Figure 17, the collapse position of shells was affected by eigenmodes and was stochastic; these phenomena might result from the sensitive structure of sphere-segmented toroidal shells under the number of segments from 1–6. Since single spherical shells [51] have been proven to have closely spaced eigenvalues, sphere-segmented toroidal shells designed using the principle of consistent deformation might have closely spaced eigenvalues.

Completeness exerted a small effect on the buckle loads of sphere-segmented toroidal shells. As indicated in Table 6, the nonlinear buckling load of perfect toroidal shells ranged from 12.350 to 12.753 MPa. Under small imperfection size, the nonlinear buckling load ranged from 10.186 to 10.492 MPa.

4. Conclusions

In this study, sphere-segmented toroidal shells were designed, based on structure optimization results related to bi-segmented spherical shells. The buckling characteristics of sphere-segmented toroidal shells were proposed, based on numerical and experimental methods. The main conclusions are as follows:

(1) The deviation between the experimental and numerical analysis results was within a reasonable range (12.8–13.9%). The collapse position of numerical analysis and the hydrostatic test of ST-1 was consistent. The numerical analysis results of ST-2 sphere-segmented toroidal shells were different from the hydrostatic test, because the welding imperfections, stiffness, geometric properties, and thickness were different in the collapse location.

(2) The proposed sphere-segmented toroidal shells are highly imperfection-sensitive structures with closely spaced eigenvalues. The minimum deviation of the eigenvalues of adjacent orders was 0, the maximum deviation was only 0.0038%, and the linear buckling load varied from 26.549 to 26.758 MPa. Imperfection sensitivity analysis verified that the sphere-segmented toroidal shell was a sensitive structure.

(3) For a nonlinear analysis, the numerical analysis results under the first eigenmode were consistent with the worst eigenmode imperfection. The post-buckling modes of the sphere-segmented toroidal shells were all localized dents. A deviation of only 2.2% was noted between nonlinear buckling loads under the effect of the first mode and the worst mode; however, the location of the imperfection was different.

(4) The trend of the equilibrium path for sphere-segmented toroidal shells is consistent with that for spherical shells, revealing instability. The post-buckling mode instability occurred near the ring, due to geometric imperfection, which is typical for a hemisphere subjected to external pressure. The post-buckling mode instability occurred on the sym-

metry plane of the sphere, due to incomplete welding, which is typical for a single sphere subjected to external pressure.

(5) Ellipticity exerted a negligible effect on the buckling loads of sphere-segmented toroidal shells. The deviation in various loads of sphere-segmented toroidal shells under the effect of ellipticity was in the range of 0.1–3.6%. The trend of the equilibrium paths of the four models with different ellipticities was consistent with the manufactured models, and all equilibrium paths of the four models exhibited instability. Similarly, completeness had a negligible effect on the buckling loads of sphere-segmented toroidal shells under a scenario of small imperfections. The nonlinear buckling load ranged from 10.186 to 10.492 MPa. The post-buckling modes exhibited unpredictability, owing to the presence of closely spaced eigenvalues. The eigenmode of a sphere-segmented toroidal shell with different segment numbers took the form of multiple waves.

Author Contributions: Conceptualization, J.Z.; methodology, C.D. and J.Z.; software, J.Z. and Y.Z.; validation, F.W.; formal analysis, C.D. and J.Z.; investigation, C.D. and J.Z.; data curation, C.D. and F.W.; writing—original draft preparation, C.D.; writing—review and editing, J.Z. All authors have read and agreed to the published version of the manuscript.

Funding: This work was supported by the National Natural Science Foundation of China (Grant Nos. 52071160 and 52222111).

Data Availability Statement: The data presented in this study are available on request from the corresponding author. The data are not publicly available due to privacy.

Conflicts of Interest: The authors declare no conflict of interest.

References

1. Du, Q.; Cui, W.; Zhang, B. Buckling characteristics of a circular toroidal shell with stiffened ribs. *Ocean Eng.* **2015**, *108*, 325–335. [CrossRef]
2. Ross, C. A conceptual design of an underwater missile launcher. *Ocean Eng.* **2005**, *32*, 85–99. [CrossRef]
3. Ross, C. A conceptual design of an underwater vehicle. *Ocean Eng.* **2006**, *33*, 2087–2104. [CrossRef]
4. Błachut, J. Collapse tests on externally pressurized toroids. *J. Press. Vessel. Technol. Trans. ASME* **2003**, *125*, 91–96. [CrossRef]
5. Błachut, J. Buckling and first ply failure of composite toroidal pressure hull. *Comput. Struct.* **2004**, *82*, 1981–1992. [CrossRef]
6. Błachut, J.; Jaiswal, O. Instabilities in torispheres and toroids under suddenly applied external pressure. *Int. J. Impact Eng.* **1999**, *22*, 511–530. [CrossRef]
7. Zingoni, A.; Enoma, N.; Govender, N. Equatorial bending of an elliptic toroidal shell. *Thin-Walled Struct.* **2015**, *96*, 286–294. [CrossRef]
8. Enoma, N.; Zingoni, A. Analytical formulation and numerical modelling for multi-shell toroidal pressure vessels. *Comput. Struct.* **2020**, *232*, 105811. [CrossRef]
9. Du, Q.; Cui, W.; Wan, Z. Nonlinear Finite Element Analysis of a Toroidal Shell with Ring-Stiffened Ribs. *OMAE* **2010**, *21088*, 759–765. [CrossRef]
10. Du, Q.; Zou, G.; Zhang, B.; Wan, Z. Simplified theoretical solution of circular toroidal shell with ribs under uniform external pressure. *Thin-Walled Struct.* **2015**, *96*, 49–55. [CrossRef]
11. Moradi-Dastjerdi, R.; Behdinan, K.; Safaei, B.; Qin, Z. Buckling behavior of porous CNT-reinforced plates integrated between active piezoelectric layers. *Eng. Struct.* **2020**, *222*, 111141. [CrossRef]
12. Civalek, Ö.; Avcar, M. Free vibration and buckling analyses of CNT reinforced laminated non-rectangular plates by discrete singular convolution method. *Eng. Comput.* **2020**, *38*, 489–521. [CrossRef]
13. Zhang, J.; Di, C.; Wang, F.; Tang, W. Buckling of segmented toroids under external pressure. *Ocean Eng.* **2021**, *239*, 109921. [CrossRef]
14. Zhang, R.; Zhang, W.; Yuan, S. Research on hydro-forming of spherical shells with different preform types. *Int. J. Adv. Manuf. Technol.* **2017**, *92*, 2631–2638. [CrossRef]
15. Evkin, A.; Lykhachova, O. Design buckling pressure for thin spherical shells: Development and validation. *Int. J. Solids Struct.* **2019**, *156–157*, 61–72. [CrossRef]
16. Cui, W. An Overview of Submersible Research and Development in China. *J. Mar. Sci. Appl.* **2018**, *17*, 459–470. [CrossRef]
17. Yu, C.; Chen, Z.; Chen, C.; Chen, Y. Influence of initial imperfections on ultimate strength of spherical shells. *Int. J. Nav. Arch. Ocean Eng.* **2017**, *9*, 473–483. [CrossRef]
18. Liang, C.; Shiah, S.W.; Jen, C.; Chen, H. Optimum design of multiple intersecting spheres deep-submerged pressure hull. *Ocean Eng.* **2004**, *31*, 177–199. [CrossRef]

19. Gou, P.; Cui, W. Study of structural optimization problem for multiple intersecting spherical pressure hulls. *Chuan Bo Li Xue/J. Sh. Mech.* **2009**, *13*, 269–277.
20. Zhang, M.; Tang, W.; Wang, F.; Zhang, J.; Cui, W.; Chen, Y. Buckling of bi-segment spherical shells under hydrostatic external pressure. *Thin-Walled Struct.* **2017**, *120*, 1–8. [CrossRef]
21. Liu, J.; Yu, B.; Zhou, Y.; Zhang, Y.; Duan, M. The buckling of spherical-cylindrical composite shells by external pressure. *Compos. Struct.* **2021**, *265*, 113773. [CrossRef]
22. Sobhani, E.; Masoodi, A. A comprehensive shell approach for vibration of porous nano-enriched polymer composite coupled spheroidal-cylindrical shells. *Compos. Struct.* **2022**, *289*, 115464. [CrossRef]
23. Sobhani, E.; Masoodi, A.; Ahmadi-Pari, A. Wave frequency responses estimate of the nanocomposite linked hemispherical-conical shell underwater-like bodies with the impacts of two types of graphene-based nanofillers. *Ocean Eng.* **2022**, *262*, 112329. [CrossRef]
24. Sobhani, E.; Masoodi, A.; Ahmadi-Pari, A. Circumferential vibration analysis of nano-porous-sandwich assembled spherical-cylindrical-conical shells under elastic boundary conditions. *Eng. Struct.* **2022**, *273*, 115094. [CrossRef]
25. Sobhani, E.; Masoodi, A.; Dimitri, R.; Tornabene, F. Free vibration of porous graphene oxide powder nano-composites assembled paraboloidal-cylindrical shells. *Compos. Struct.* **2023**, *304*, 116431. [CrossRef]
26. Rezaiee-Pajand, M.; Masoodi, A. Shell instability analysis by using mixed interpolation. *J. Braz. Soc. Mech. Sci. Eng.* **2019**, *41*, 419. [CrossRef]
27. Zingoni, A.; Mokhothu, B.; Enoma, N. A theoretical formulation for the stress analysis of multi-segmented spherical shells for high-volume liquid containment. *Eng. Struct.* **2015**, *87*, 21–31. [CrossRef]
28. Zhang, J.; Hu, H.; Wang, F.; Li, Y.; Tang, W. Buckling of externally pressurized torispheres with uniform and stepwise thickness. *Thin-Walled Struct.* **2022**, *173*, 109045. [CrossRef]
29. Zhang, J.; Wang, Y.; Wang, F.; Tang, W. Buckling of stainless steel spherical caps subjected to uniform external pressure. *Ships Offshore Struct.* **2018**, *13*, 779–785. [CrossRef]
30. Zhang, J.; Wang, Y.; Tang, W.; Zhu, Y.; Zhao, X. Buckling of externally pressurised spherical caps with wall-thickness reduction. *Thin-Walled Struct.* **2019**, *136*, 129–137. [CrossRef]
31. Zhang, J.; Zhang, Y.; Wang, F.; Zhu, Y.; Cui, W.; Chen, Y. Experimental and numerical studies on the buckling of the hemispherical shells made of maraging steel subjected to extremely high external pressure. *Int. J. Press. Vessel. Pip.* **2019**, *172*, 56–64. [CrossRef]
32. Zhang, J.; Lin, Z.; Wang, F.; Zhao, T.; Zhu, Y. Ultimate strength of externally pressurised steel spheres containing through-thickness defects. *Int. J. Press. Vessel. Pip.* **2022**, *199*, 104750. [CrossRef]
33. Schalen, A. *EN 1993-1.6: 2007.E*; Eurocode 3—Design of Steel Structures—Part 1–6: Strength and Stability of Shell Structures. European Committee for Standardisation: Brussels, Belgium, 2004.
34. CCS. *Rules for Construction and Classification of Diving Systems and Submersibles*; China Classification Society: Beijing, China, 2018.
35. Ricks, E. An Incremental approach to the Solution of snapping and buckling problems. *Int. J. Solids Struct.* **1979**, *15*, 529–551. [CrossRef]
36. Zhang, J.; Wang, M.; Wang, W.; Tang, W. Buckling of egg-shaped shells subjected to external pressure. *Thin-Walled Struct.* **2017**, *113*, 122–128. [CrossRef]
37. Zhang, J.; Tan, J.; Tang, W.; Zhao, X.; Zhu, Y. Experimental and numerical collapse properties of externally pressurized egg-shaped shells under local geometrical imperfections. *Int. J. Press. Vessel. Pip.* **2019**, *175*, 103893. [CrossRef]
38. Zhang, J.; Hua, Z.; Wang, F.; Tang, W.; Zhu, Y. Buckling of an egg-shaped shell with varying wall thickness under uniform external pressure. *Ships Offshore Struct.* **2019**, *14*, 559–569. [CrossRef]
39. Zhang, J.; Zhang, M.; Tang, W.; Wang, W.; Wang, M. Buckling of spherical shells subjected to external pressure: A comparison of experimental and theoretical data. *Thin-Walled Struct.* **2017**, *111*, 58–64. [CrossRef]
40. Zhang, J.; Huang, C.; Wagner, H.; Cui, W.; Tang, W. Study on dented hemispheres under external hydrostatic pressure. *Mar. Struct.* **2020**, *74*, 102819. [CrossRef]
41. Zhang, J.; Wang, X.; Tang, W.; Wang, F.; Zhu, Y. Non-linear collapse behavior of externally pressurized resin toroidal and cylindrical shells: Numerical and experimental studies. *Ships Offshore Struct.* **2021**, *16*, 529–545. [CrossRef]
42. Zhang, J.; Wang, X.; Tang, W.; Wang, F.; Yin, B. Experimental and numerical buckling analysis of toroidal shell segments under uniform external pressure. *Thin-Walled Struct.* **2020**, *150*, 106689. [CrossRef]
43. Reitinger, R.; Ramm, E. Buckling and imperfection sensitivity in the optimization of shell structures. *Thin-Walled Struct.* **1995**, *23*, 159–177. [CrossRef]
44. Deml, M.; Wunderlich, W. Direct evaluation of the "worst" imperfection shape in shell buckling. *Comput. Methods Appl. Mech. Eng.* **1997**, *149*, 201–222. [CrossRef]
45. Lindgaard, E.; Lund, E.; Rasmussen, K. Nonlinear buckling optimization of composite structures considering "worst" shape imperfections. *Int. J. Solids Struct.* **2010**, *47*, 3186–3202. [CrossRef]
46. Dey, T.; Ramachandra, L. Computation of worst geometric imperfection profiles of composite cylindrical shell panels by minimizing the non-linear buckling load. *Appl. Math Model.* **2019**, *74*, 483–495. [CrossRef]
47. Magisano, D.; Garcea, G. Increasing the buckling capacity with modal geometric "imperfections" designed by a reduced order model. *Thin-Walled Struct.* **2022**, *178*, 109529. [CrossRef]
48. Zhang, J.; Zhang, S.; Cui, W.; Zhao, X.; Tang, W.; Wang, F. Buckling of circumferentially corrugated cylindrical shells under uniform external pressure. *Ships Offshore Struct.* **2019**, *14*, 879–889. [CrossRef]

49. Lee, A.; Jiménez, F.; Marthelot, J.; Hutchinson, J.; Reis, P. The Geometric Role of Precisely Engineered Imperfections on the Critical Buckling Load of Spherical Elastic Shells. *J. Appl. Mech. Trans. ASME* **2016**, *83*, 111005. [CrossRef]
50. Castro, S.; Zimmermann, R.; Arbelo, M.; Khakimova, R.; Hilburger, M.; Degenhardt, R. Geometric imperfections and lower-bound methods used to calculate knock-down factors for axially compressed composite cylindrical shells. *Thin-Walled Struct.* **2014**, *74*, 118–132. [CrossRef]
51. Hutchinson, J. Buckling of spherical shells revisited. *Proc. R. Soc. A Math. Phys. Eng. Sci.* **2016**, *472*, 20160577. [CrossRef]